Vol. 08, No. 3 (2026) 1673-1688, doi: 10.24874/PES08.03.021

Proceedings on Engineering Sciences

www.pesjournal.net

SURFACE MODIFICATION OF LPBF-FABRICATED 316L STAINLESS STEEL USING SHOT PEENING: WETTABILITY AND CORROSION PERFORMANCE FOR BIOMEDICAL IMPLANTS

Mariya Das Gurram[1]
Vishnu Vardhana Naidu B

Received 13.06.2026
Revised 16.07.2026
Accepted 21.08.2026

Keywords:

Laser Powder Bed Fusion (LPBF), 316L stainless steel, Shot peening; Wettability, Corrosion resistance.

A B S T R A C T

This study investigates the effect of shot peening (SP) processing times of 6 min (SP6), 8 min (SP8), and 10 min (SP10) on the surface wettability and electrochemical corrosion behavior of laser powder bed fusion (LPBF)-fabricated 316L stainless steel (316L SS) for biomedical implant applications. While LPBF allows for complex, customized implant fabrication, as-printed (AP) components suffer from high surface roughness, residual porosity, and tensile residual stresses that compromise corrosion resistance and biocompatibility. To resolve these issues, SP was applied to induce severe plastic deformation and refine the near-surface microstructure. Surface properties and electrochemical performance were evaluated using FESEM, Optical Microscopy, contact angle measurements (in DI water and PBS), potentiodynamic polarization, and electrochemical impedance spectroscopy (in 0.5 M NaCl). SP successfully refined the microstructure, minimized surface defects, and introduced beneficial compressive residual stresses, producing condition-dependent changes in surface wettability. Contact angles ranged from 26.23±1.85° to 75.26±2.78° in DI water and from 73.08±2.84° to 88.60±3.10° in PBS under the treated condition. All investigated surfaces remained hydrophilic, with contact angles below 90°. Furthermore, corrosion resistance improved progressively in the order of SP10 > SP8 > SP6 > AP. The SP10 specimen exhibited the lowest corrosion rate (decreasing from 8.907±1.02 *mpy to* 2.103±0.55 *mpy) and a substantial increase in charge-transfer resistance (10100 Ω·cm²) as indicated by PDP and EIS results. Overall, shot peening improved the surface and corrosion resistance of LPBF 316L stainless steel, with the best conditions depending on the desired performance. More in vitro and long-term studies are needed to confirm its suitability for biomedical implants.*

© 2026 Published by Faculty of Engineering

[1] Corresponding author: Mariya Das Gurram
Email: mariyadas2000@gmail.com

1. INTRODUCTION

Laser Powder Bed Fusion (LPBF) is a leading metal additive manufacturing technology that enables the fabrication of complex geometries, internal channels, and patient-specific components that are difficult to produce using conventional subtractive methods (Nizam et al., 2024; Gibson et al., 2021). By selectively melting successive powder layers with a high-energy laser, LPBF produces near-net-shape components with high dimensional accuracy and minimal material waste (Gibson et al., 2021), supporting applications in the aerospace, automotive, energy, and biomedical sectors (Frazier, 2014). However, the structural reliability and long-term performance of LPBF components depend strongly on their microstructure and surface integrity, which are governed by the process's intense thermo-mechanical history (DebRoy et al., 2018; Bagehorn et al., 2017).

AISI 316L austenitic stainless steel (316L SS) is widely used for its favorable strength, ductility, corrosion resistance, biocompatibility, and cost-effectiveness (Li et al., 2024). Its Cr-, Ni-, and Mo-containing composition promotes the formation of a protective passive oxide film, providing resistance to aggressive physiological environments (Sangoi et al., 2025; Bae et al., 2022). Consequently, 316L SS is used in orthopedic hardware, trauma implants, cardiovascular stents, and dental devices (Bae et al., 2022; Chabak et al., 2021). LPBF further enables customized implants with tailored porosity and complex geometries (Chabak et al., 2021; Sun Z. et al., 2024).

The rapid melting and solidification inherent to LPBF, with cooling rates of approximately 10^4–10^7 K s^{-1} (Diaz Vallejo et al., 2021), produce a characteristic hierarchical microstructure comprising overlapping melt pools, fine cellular/columnar austenitic structures, elemental segregation, and high dislocation densities (Barode et al., 2025; Sun F. et al., 2024). However, depending on processing parameters and powder characteristics (Guillen et al., 2024; Aziz et al., 2025), the process can also generate tensile residual stresses, partially melted particles, balling, lack-of-fusion defects, gas porosity, and high surface roughness (Guillen et al., 2024; Agrawal & Thoma, 2022). These surface irregularities and microstructural heterogeneities can compromise functional performance (Agrawal & Thoma, 2022; Jagannati et al., 2025). In particular, partially fused particles, staircase features, and surface-connected pores act as stress concentrators that accelerate fatigue-crack initiation (Bagehorn et al., 2017; Jagannati et al., 2025; MariyaDas & Naidu, 2026) and disrupt passive-film continuity, increasing susceptibility to localized corrosion (Sangoi et al., 2025; Bae et al., 2022). Surface characteristics may also influence biological interactions relevant to implant performance (Nizam et al., 2024; Chabak et al., 2021). Therefore, improving surface integrity is essential for expanding the biomedical application of LPBF-fabricated 316L SS (DebRoy et al., 2018; Mahmood et al., 2022).

Various post-processing methods, including machining, abrasive finishing, laser polishing, chemical/electrochemical polishing, hot isostatic pressing, and heat treatment, have been used to improve LPBF surfaces. However, these approaches may add manufacturing complexity, incur high costs, cause dimensional changes, or induce thermally driven microstructural modifications (Mahmood et al., 2022). Surface severe plastic deformation (SSPD) techniques offer an alternative by primarily modifying the near-surface region while largely preserving the refined LPBF bulk microstructure. Conventional and severe shot peening, ultrasonic shot peening, ultrasonic nanocrystal surface modification, and laser shock peening can introduce grain refinement, high dislocation densities, and compressive residual stresses (Venumurali et al., 2025; Basha et al., 2024; Haribaskar & Sampath Kumar, 2024), thereby improving hardness, wear resistance, and fatigue performance (Bagehorn et al., 2017; Chen et al., 2025).

Among these techniques, shot peening (SP) is particularly attractive for its simplicity, cost-effectiveness, scalability, and applicability to complex geometries. Repeated impacts from high-velocity spherical media induce severe localized plastic deformation, flatten surface asperities and partially melted particles, close shallow, surface-connected defects, and generate compressive residual stresses (Chen et al., 2025; Venumurali et al., 2024; MariyaDas & Naidu, 2026). At the microstructural level, SP promotes dislocation multiplication and rearrangement into cells and subgrain boundaries, which may evolve toward refined grain structures. Depending on alloy stability and peening intensity, deformation twinning and strain-induced martensitic transformation may also occur, contributing to strengthening and improved surface performance (Chen et al., 2025; Venumurali et al., 2024).

SP-induced topographical and microstructural changes can also alter surface wettability, which is governed by the combined effects of surface morphology, oxide chemistry, and near-surface structure (Haribaskar & Sampath Kumar, 2024; Chen et al., 2025). Because surface wettability can influence liquid spreading, protein adsorption, and subsequent cell–surface interactions (Nizam et al., 2024; Venumurali et al., 2024; Barberi & Spriano, 2021), contact-angle measurements provide useful information for evaluating surface modification. Moderately hydrophilic surfaces with contact angles below 90° are generally considered favorable for balancing protein adsorption and cellular interactions (Venumurali et al., 2024; Barberi & Spriano, 2021; Thangaraj et al., 2015).

Electrochemical stability is equally important because chloride-containing physiological environments can trigger localized corrosion when the passive film is disrupted by surface defects, inclusions, or residual stresses (Sangoi et al., 2025; Chabak et al., 2021). LPBF-induced roughness and porosity can further promote the initiation of localized corrosion (Sangoi et al., 2025), whereas appropriate surface modification may reduce surface defects and enhance passive-film stability (Thangaraj et al., 2015). Excessive peening, however, may introduce microscale damage or highly deformed surface regions that adversely affect corrosion resistance (Thangaraj et al., 2015). Optimizing peening duration is therefore important for achieving a suitable balance among surface integrity, wettability, and electrochemical performance (Yazdani et al., 2024).

Despite extensive research on LPBF 316L SS and shot peening (Haribaskar & Sampath Kumar, 2024), systematic investigations of how SP duration affects the concurrent evolution of surface roughness, microstructure, wettability, and corrosion behavior remain limited. Previous studies have examined peening-induced changes in electrochemical and wetting characteristics (Yazdani et al., 2024) or peening duration in conventionally manufactured 316L alloys; however, comprehensive correlations among severe plastic deformation, wettability, and electrochemical performance in LPBF-fabricated biomedical 316L SS remain insufficiently established (Haribaskar & Sampath Kumar, 2024; Mofazali et al., 2025).

The novelty of this study lies in systematically establishing the previously unexplored relationship among shot-peening duration (6, 8, and 10 min), surface wettability, and the electrochemical corrosion behavior of LPBF-fabricated 316L SS. Unlike the authors' previous work (MariyaDas & Naidu, 2026), which focused on surface, microstructural, and residual-stress characteristics, the present study correlates these SP-induced modifications with contact-angle response, polarization behavior, electrochemical impedance, corrosion rate, and post-corrosion surface features. This integrated approach reveals how peening duration governs the processing–structure–wettability–corrosion relationship and identifies a suitable SP condition for biomedical surface applications.

2. MATERIALS AND METHODS

2.1. Feedstock Material and LPBF Fabrication

The feedstock material used in this study was biomedical-grade AISI 316L stainless steel powder supplied by INDO-MIM, Bangalore, India, with a spherical particle size distribution of 15-53 µm to ensure high powder flowability, uniform build rates, and consistent green density during LPBF. The chemical composition of the as-received powder was verified against the supplier's certified material datasheet and confirmed to comply with ASTM F3184-16. (ASTM F3184-16 Standard Specification for Additive Manufacturing Stainless Steel Alloy, 2024) (Table 1).

Table 1. Chemical composition of SS316L powder utilized for the present work (in wt.%)

Element	C	Si	Mn	Cr	Ni	Mo	P	S	Fe
Datasheet	0.03	0.75	2.00	16.0 – 18.0	10.0 – 14.0	2.00-3.00	0.045	0.030	Bal
EDS	<0.03	0.2	1.00	14.38	6.65	2.00	0.01	0.01	Bal
ASTM F3184-16	0.030	1.00	2.00	16.00-18.00	10.00-14.00	2.00-3.00	0.045	0.030	Bal

The certified bulk composition served as the primary baseline for material-grade identification. Subsequent microstructural morphology and localized elemental characterization were conducted using Field Emission Scanning Electron Microscopy (FESEM, Zeiss GmbH, Germany) equipped with Energy Dispersive X-ray Spectroscopy (EDS, Oxford Instruments), as shown in Figures 1(a) and 1(b).

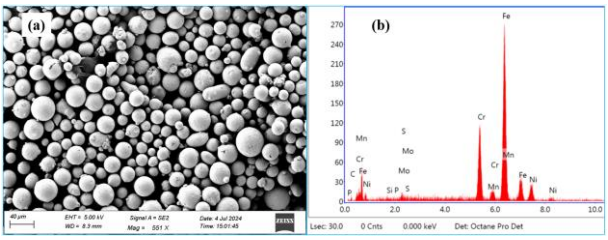


Figure 1. SEM characterization of 316L SS powder: (a) powder-particle morphology and (b) corresponding EDS spectrum showing the elemental composition

Standard dimensioned samples for microstructural evolution, surface roughness, contact angle measurements, and electrochemical corrosion testing are fabricated via the LPBF route on the EOS M 290 3D printing machine (GmbH, Germany) under a high-purity argon atmosphere to maintain the oxygen level below 0.1% and prevent oxidation, using optimized process parameters reported by Basha & Sankar (2023), which are provided in Table 2, and the flow work diagram of this process is shown in Figure 2.

Table 2. Optimized LPBF processing parameters used for the fabrication of 316L SS samples, adopted from Basha & Sankar (2023)

S No	Parameter	Value
1	Laser Power (Yb fiber laser)	200W
2	Hatch Distance	140 µm
3	Layer Thickness	60 µm
4	Exposure Time	100 µs
5	Point Distance	40 µm
6	Scan Strategy	XY
7	Scan Rotation Angle between Layers	47°
8	Build Orientation	XY 15°
9	Build Plate Volume	250 × 250 × 50 mm

After fabrication, the specimens were carefully machined using a WireCut Electric Discharge Machine (WEDM) (Concord CNC WireCut EDM DK7732VC, Bangalore, India) to remove them from the build plate.

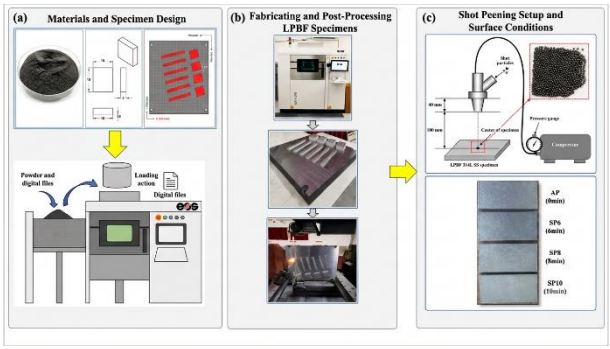


Figure 2. Schematic of the experimental workflow: (a) AISI 316L SS powder, CAD model (10 × 10 × 3 mm), and LPBF build layout; (b) LPBF specimen fabrication and subsequent sample removal; and (c) shot-peening treatment and resulting surface conditions of the AP, SP6, SP8, and SP10 samples

2.2. Surface Modification via Shot Peening

The as-printed samples were ultrasonically cleaned in acetone and ethanol, immediately removed from the build plate, and then subjected to SP at room temperature using a 6-axis industrial robot with a pneumatic blast machine that directed spherical shots through a nozzle onto the samples. The processing parameters were systematically tailored to achieve uniform surface coverage, and the primary variables used during the treatment are summarized in Table 3.

Table 3. Shot-peening process parameters used for the surface treatment of LPBF 316L SS samples

Parameter	Value / Details
Shot Media Type	Cast Steel-S390G
Hardness of shot media	48 to 52 HRC
Shot Diameter	0.8 to 1 mm
Almen Intensity (A strip)	0.5 mm A
Air Pressure	6.5 bar
Surface Coverage	100%
Velocity of shots	110 m/s
Nozzle Distance & Angle	100 mm at 60° to the surface

All other operating parameters remained constant throughout the shot-peening process. The samples were designated AP (as-printed/0 min shot peening), SP6 (6 min), SP8 (8 min), and SP10 (10 min). An A-type Almen strip with a reference intensity of 0.5 mmA, as reported in Table 3, was used to determine the Almen intensity and corresponding arc height for each shot-peening condition, following the procedure described by Kirk & Coventry (2012). The Almen strips were exposed under the respective peening conditions, and the resulting curvature was measured with an Almen gauge. The measured Almen intensity values for SP6, SP8, and SP10 were 4.54, 4.56, and 4.81 mmA, respectively, with corresponding arc heights of 0.16, 0.18, and 0.33 mm. The AP condition was not shot peened and therefore served as the untreated reference condition.

2.3. Microstructural and Topographical Characterization

After SP, the surface morphology of all samples (AP, SP6, SP8, and SP10) was analyzed using scanning electron microscopy (SEM; Tescan Vega-3, Czech Republic). X-ray diffraction (XRD) measurements of the raw powder, As-Printed (APed), and Shot peened (SPed) samples employed a Bruker D8 Advance diffractometer (CuKα, λ = 1.5406 Å, 40 kV, 25 mA, 2θ = 20°–90°), with peak broadening assessed via X'Pert HighScore Plus software. Residual stress levels were determined using an iXRD Proto diffractometer (Mn Kα, $\sin^2\psi$ method; ASTM E2860-20) at three locations per sample, with settings of 25 kV and 4 mA. To investigate the impact of plastic deformation on surface topography, a 3D optical profilometer (Bruker Contour X200, USA) was used to measure surface roughness at three locations on each sample under each condition, and the data were reported as mean ± SD for further analysis. Importantly, these combined techniques provided a detailed understanding of both surface visual features and quantitative changes in roughness caused by shot peening.

The LPBF fabrication and shot-peening conditions followed those reported in our previous study (MariyaDas & Naidu, 2026), whereas the wettability and electrochemical corrosion investigations presented here constitute the additional experimental scope of the present study.

2.4. Surface Wettability Measurements

A goniometer (Attension Theta, Biolin Scientific AB, Sweden) with a high-resolution camera (~5 MP) was used to measure the droplet contact angle between the sample surface and the liquid for two media: deionized water (DI W) and phosphate-buffered saline (PBS) at pH 7.2 to assess surface wettability behaviour. Before testing, clean specimens by immersing them in alcohol, then rinse them with distilled water and dry them. The sessile drop technique was used to measure contact angles; a 6 µL droplet was precisely metered and deposited onto each surface, and its profile was immediately captured by the integrated high-resolution camera for automated geometric analysis.
The procedure was consistently applied to three measurements taken at different locations on each specimen per condition within each medium; therefore, these measurements represent spatial or technical replicates rather than independent biological or experimental specimens. Accordingly, the data are reported as mean ± SD, and no inferential statistical comparison between treatment conditions was performed because independent specimen-level replication was not available.

2.5. Electrochemical Corrosion Evaluation

The corrosion behaviour of the AP and shot-peened surfaces was evaluated electrochemically in a 0.5 M NaCl solution at ambient temperature using a CH-660E electrochemical workstation with a conventional three-electrode cell. The LPBF 316L SS specimen served as the working electrode with an exposed area of 1 cm², while a saturated calomel electrode (SCE) and platinum mesh served as the reference and counter electrodes, respectively.

Before electrochemical testing, the open-circuit potential (OCP) was monitored for 400 s to allow the metal/electrolyte interface to approach a quasi-stable state. Potentiodynamic polarization (PDP) measurements were then performed over a potential range of ±250 mV relative to the OCP measured at the end of the 400 s monitoring period, using a scan rate of 10 mV/s. Electrochemical impedance spectroscopy (EIS) was conducted with a ±5 mV sinusoidal AC perturbation over a frequency range of 100 kHz–1 Hz. The impedance data were evaluated using Nyquist and Bode plots (magnitude and phase angle) and fitted to the (Q(R(Q(RW)))) equivalent electrical circuit with Z-Simp Win software to determine the electrochemical parameters. Because the lower-frequency limit was 1 Hz, the EIS results were used primarily for comparative evaluation of the investigated surface conditions rather than for complete characterization of long-term passive-film or diffusion-controlled processes. All electrochemical measurements were performed three times for each condition, and the results were reported as mean ± standard deviation (SD), where applicable, to assess experimental reproducibility.

3. RESULTS AND DISCUSSIONS

3.1 Topography and Microstructural Evaluation

The surface morphology, roughness, and microstructural characteristics presented in this section are based on the same material system investigated in our previous study (MariyaDas & Naidu, 2026). Although selected baseline observations were reported previously, the present study includes additional analysis, revised characterization, and expanded interpretation of these features to establish their relationship to the newly investigated wettability and electrochemical corrosion behavior.

Figure 3 shows the edge effects of the different LPBF 316L SS samples, namely AP (a), SP6 (b), SP8 (c), and SP10 (d), as observed under optical microscopy. The AP condition exhibits partially melted particles, lack-of-fusion features, and other inherent LPBF characteristics.

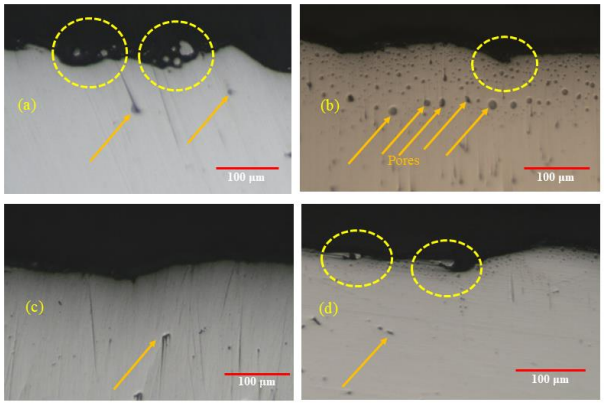


Figure 3. Optical microscopy images of LPBF 316L SS in the (a) as-printed (AP), (b) SP6, (c) SP8, and (d) SP10 conditions. The figure was adapted from the dataset in our previous study (MariyaDas & Naidu, 2026) and modified for this analysis.

This high concentration of surface defects is a well-documented artifact of the LPBF thermal cycle and the mechanics of powder melting (Guillen et al., 2024; Agrawal & Thoma, 2022; Yadroitsev & Smurov, 2011). Consequently, the AP sample exhibits the highest surface roughness, measured at 107.81 ± 6.47 µm, as shown in Figure 4, with numerous surface asperities, as do the shot-peened samples.

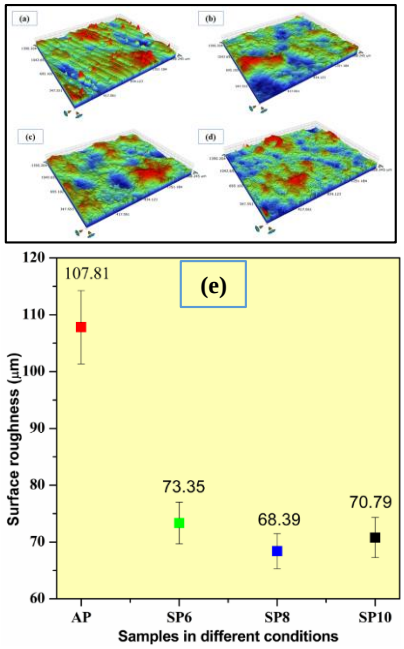


Figure 4. Optical profilometry images of LPBF 316L SS samples: (a) AP, (b) SP6, (c) SP8, (d) SP10, with (e) Surface roughness (R_z) comparison. Based on data from (MariyaDas & Naidu, 2026), including profilometry images and a new roughness comparison

These characteristic surface features and the distinctive surface microstructure of the AP condition are further illustrated in Figure 5 (a).

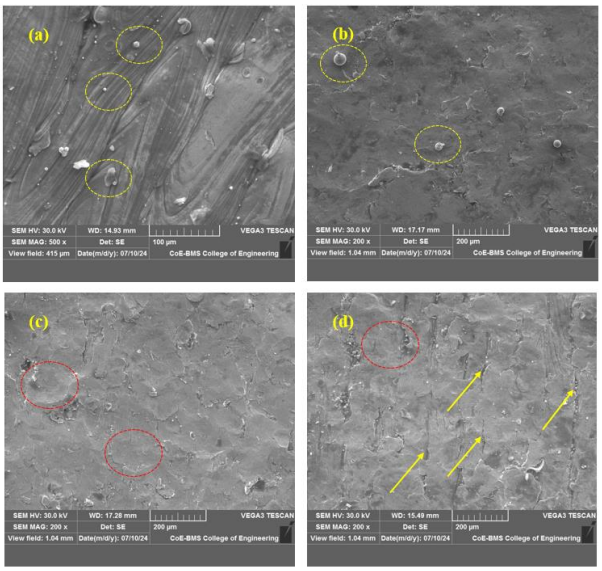


Figure 5. SEM micrographs of LPBF 316L SS samples under the (a) AP, (b) SP6, (c) SP8, and (d) SP10 conditions. Based on the characterization dataset associated with MariyaDas & Naidu (2026), with the micrographs modified and presented in the current study

After 6 min of SP, the partially melted particles and other asperities are moderately flattened, reducing the surface roughness to 73.35±3.67 µm. This indicates that the peening treatment was sufficient to modify the near-surface layer and partially smooth the original LPBF surface without causing excessive surface disturbance. This initial stage aligns with established peening mechanics, in which high-velocity media preferentially flatten prominent surface features through localized plastic deformation (Mahmood et al., 2022; Chen et al., 2025; Venumurali et al., 2024). With further peening, the SP8 sample shows a more pronounced reduction in roughness, reaching 68.39±3.08 µm. In this condition, the shot-peening action effectively removes additional surface asperities and helps close surface pores, producing a smoother, more uniform surface. This suggests that SP8 provides the most favorable balance between surface smoothing and controlled surface modification.

In contrast, the SP10 sample, peened for 10 min, shows the reappearance of some asperities, which may be attributed to over-peening and the embedding of shot particles, as observed in Figure 3(d), and the value slightly increased to 70.79±3.54 µm compared to SP8. Hence, increasing peening exposure generally increases plastic deformation and compressive residual stresses, but excessive peening can damage surface integrity through high-energy impacts. Kirk (1999) emphasized controlling shot-peening intensity and duration to prevent damage. The slight increase in surface roughness at longer peening times may result from over-peening, where continued impacts offer limited benefit and cause localized damage or roughening.

However, the subsurface pores are effectively closed, which creates a continuous surface barrier that contributes to increased corrosion resistance by eliminating localized pitting initiation sites (Lodhi et al., 2018; Alharbi, 2023). Therefore, the results indicate that the surface roughness initially decreases with increasing peening duration, reaches an optimum at SP8, and then slightly increases at SP10 due to over-processing.

Overall, the optical microscopy observations confirm that shot peening progressively modifies the LPBF 316L edge morphology by reducing asperities, altering the near-surface microstructure, and introducing compressive residual stresses as reported in Table 4. Among the investigated conditions, SP8 appears to be the most effective in achieving the best compromise between roughness reduction and surface integrity (Haribaskar & Sampath Kumar, 2024; MariyaDas & Naidu, 2026; Alharbi, 2023).

The SEM micrographs (Figure 5) show a progressive change in the LPBF surface as shot-peening duration increases. The AP sample exhibits clear LPBF track marks and numerous unmelted and partially melted particles, which are highlighted by the yellow circles; these surface features are characteristic artifacts of LPBF process kinetics and powder consolidation (Guillen et al., 2024; Agrawal & Thoma, 2022; Yadroitsev & Smurov, 2011).

After 6 min of SP, some of these particles are removed, and the surface becomes more compact, while the yellow circles still indicate a few remaining particles, demonstrating the initial flattening of prominent asperities through severe plastic deformation (Mahmood et al., 2022; Basha et al., 2024; Venumurali et al., 2024).

At 8 min, the surface exhibits more uniformly distributed plastic deformation, while the red circles highlight regions of overlapping shot-induced indentations. These morphological features indicate increased surface modification and a more uniform surface appearance than that observed at shorter shot-peening durations (Chen et al., 2025; Haribaskar & Sampath Kumar, 2024).

At 10 min, excessive peening results in over-peening, with the red-circled areas showing pronounced indentation overlap and the blue arrows indicating microcracks formed by repeated impacts and localized fatigue (Alharbi, 2023; Walczak et al., 2024).
Overall, the arrow marks and circles clearly identify the transition from as-built roughness to surface smoothing, followed by microscale damage at longer peening durations, which matches the structural degradation patterns, and these observations are typically reported during prolonged SSPD (Yazdani et al., 2024).

3.2. Wettability behaviour of DI Water and PBS media

Building on the previously reported surface characterization (MariyaDas & Naidu, 2026), the present study extends the investigation to wettability behavior, which constitutes a new experimental contribution of this work.

The authors (Yazdani et al., 2024) investigated and observed that surface wettability is widely acknowledged as a key parameter affecting the corrosion response of metallic materials in aqueous environments, owing to its influence on electrolyte–surface interactions. To investigate the influence of SP on the wettability of LPBF-fabricated 316L SS, static contact angle measurements were performed using DI water and PBS separately. The corresponding droplet profiles are presented in Figure 6(a–d), while the average measured contact angles are summarized in Figure 6(e).

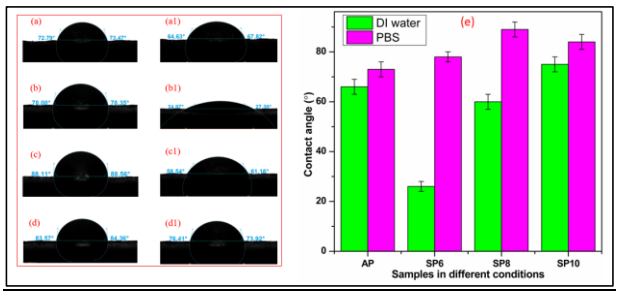


Figure 6. Optical droplet profiles and corresponding contact-angle measurements for LPBF 316L SS under AP, SP6, SP8, and SP10 conditions, using (a–d) DI water and (a1–d1) PBS, with (e) a comparison of the measured contact angles

The AP specimen exhibited baseline contact angles of 66.21±3.12° (DI W) and 73.08±2.84° (PBS). Following SP, the PBS contact angle increased progressively to 78.22±2.15° (SP6), reached a maximum of 88.60±3.10° (SP8), and then slightly decreased to 84.07±2.62° (SP10). Similarly, the DI W contact angle initially decreased to 26.23±1.85° (SP6), indicating enhanced wettability, before increasing to 59.86±2.45° (SP8) and 75.26±2.78° (SP10). Despite these variations, all measured contact angles remained below 90°, confirming that the AP and SPed surfaces retained their hydrophilic nature, which is generally considered favourable for biomedical implant applications.

The variation in wettability can be attributed to the combined effects of SP on the surface morphology and surface chemistry of LPBF 316L SS. As evidenced by the SEM micrographs (Figure 5(a)) and 3D optical profilometry (Figure 4(a)), the as-printed surface contained partially melted powder particles, staircase features, and irregular asperities characteristic of the layer-wise fabrication process. Shot peening plastically deformed these asperities, producing a more homogeneous surface with reduced roughness and uniformly distributed micro-dimples, while simultaneously introducing severe plastic deformation, grain refinement, high dislocation density, and compressive residual stresses, as investigated in the authors' previous work (MariyaDas & Naidu, 2026) and presented in Table 4. These microstructural modifications are also accompanied by changes in the surface condition, which may collectively influence the observed wetting characteristics.

Table 4. Crystallite size, microstrain, dislocation density, and residual stress of LPBF 316L SS samples under AP, SP6, SP8, and SP10 conditions. Based on the experimental data reported in our previous study (MariyaDas & Naidu, 2026), reorganized for comparison in the present investigation

Sample	AP	SP6	SP8	SP10
Crystal size (nm)	59.79	23.85	13.15	10.71
Micro-strain	1.33×10^{-3}	5.33×10^{-3}	6.31×10^{-3}	9.53×10^{-3}
Dislocation density (nm^{-2})	0.33×10^{14}	5.86×10^{14}	7.04×10^{14}	11.61×10^{14}
Residual stresses (MPa)	-48.5	-468.8	-559.1	-624

The exceptionally low DI W contact angle observed for SP6 (26.23±1.85°) suggests that moderate SP promoted rapid spreading of the water droplet on the modified surface. This behaviour is consistent with the Wenzel wetting mechanism, in which the increased effective surface area of an intrinsically hydrophilic material enhances liquid penetration into the surface texture. As the peening duration increased to SP8 and SP10, the contact angle gradually increased. This trend is consistent with the partial wetting characteristics described by the Cassie–Baxter model, in which the dense population of micro-dimples may facilitate localized air entrapment beneath the droplet, thereby reducing the effective solid–liquid contact area and increasing the apparent contact angle. However, identifying the primary wetting mechanism would require dynamic contact angle measurements or contact angle hysteresis analysis, both of which were outside the scope of this study.

The consistently higher contact angles measured with PBS than with DI W indicate that wetting behaviour was strongly influenced by liquid chemistry. Unlike deionized water, PBS contains dissolved sodium, potassium, chloride, and phosphate ions that modify interfacial interactions with the chromium-rich passive film on 316L SS, thereby reducing droplet spreading and, consequently, increasing apparent contact angles. Since PBS more closely represents the physiological environment encountered by implanted biomaterials, these measurements provide additional insight into the expected in vivo wetting behaviour.

Although SP increased the apparent contact angle, the concomitant reduction in surface roughness indicates that wettability is governed by a combination of surface topography, microstructural refinement, oxide chemistry,

and surface energy rather than by roughness alone. The transition from irregular LPBF surface features to a uniformly peened morphology altered solid–liquid interfacial interactions without changing the material's overall hydrophilic character.

The present findings are broadly consistent with Ahmed et al. (2015), who demonstrated that shot-peening parameters influence the surface roughness and wettability of AISI 316L stainless steel, thereby confirming that peening-induced surface modifications significantly affect the water contact angle.

Despite the increase in contact angle, all specimens remained within the hydrophilic regime. Similarly, Bagherifard et al. (2014) reported that shot peening-induced grain refinement significantly enhanced the surface mechanical properties and wettability of 316L SS. These improvements demonstrate the beneficial influence of shot peening on the surface characteristics, wettability, and corrosion performance (discussed in Section 3.3) of LPBF-fabricated 316L stainless steel, supporting its potential for further evaluation in orthopaedic applications.

Additionally, Figure 7 presents a schematic diagram illustrating how SP-induced surface topography influences the potential cell–surface interaction of LPBF-fabricated 316L SS. The AP surface, characterized by the highest roughness ($R_z \approx 107.81 \pm 6.47$ µm), contains irregular asperities and partially melted powder particles, which provide a limited effective contact area for initial cell anchorage.

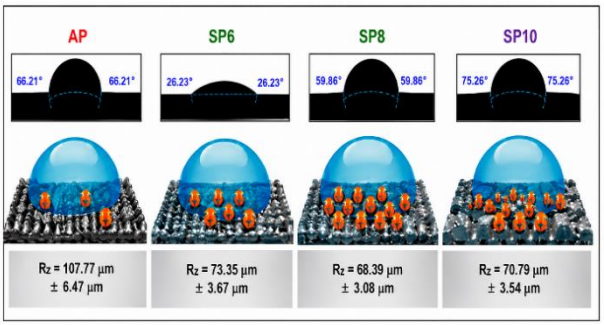


Figure 7. Schematic showing the hypothesized link between shot-peening changes in surface topography and wettability and their possible impact on surface–biological interactions of LPBF 316L SS.

SP progressively smooths the macroscale surface while introducing uniformly distributed microdimples that serve as favourable anchoring sites for proteins and cells. Consequently, the SP6 surface offers improved cell attachment due to reduced excessive roughness and the development of a more homogeneous surface morphology. Among all the conditions, SP8 ($R_z \approx 68.39 \pm 3.08$ µm) is expected to provide the most favorable environment for cell adhesion due to its optimal combination of reduced roughness, uniformly distributed micro-dimples, and stable hydrophilic behaviour, which facilitate protein adsorption and subsequent cell attachment. At the highest peening duration (SP10), slight surface deterioration from over-peening and localized damage may reduce the effectiveness of these anchoring sites, leading to marginally lower cell attachment than at SP8, despite retaining an overall favorable surface for biological interactions.

Thus, Figure 7 presents a conceptual, hypothesis-driven schematic illustrating how shot-peening-induced changes in surface topography and wettability may influence initial cell–surface interactions from AP to shot-peened conditions. Among the conditions investigated, SP8 exhibited a comparatively favorable combination of surface morphology and wettability. Surface wettability is widely recognized as a key factor influencing protein adsorption and subsequent cell–material interactions. In implant-related studies, moderately hydrophilic surfaces are frequently associated with favourable cellular responses and osseointegration (Smeets et al., 2016; Bagherifard et al., 2015). However, because no biological assays were performed in the present study, the proposed biological implications are conceptual rather than experimentally validated and require confirmation through future in vitro investigations.

3.3. Electrochemical Corrosion behaviour

Extending the previously reported surface and microstructural characterization (MariyaDas & Naidu, 2026), the present study evaluates the electrochemical corrosion behavior of AP and shot-peened LPBF 316L SS under chloride exposure.

3.3.1 Influence of microstructural evolution on the corrosion behaviour of LPBF 316L SS

The corrosion performance of LPBF-fabricated 316L SS is strongly governed by its microstructural characteristics, including process-induced defects, surface irregularities, porosity, and residual stresses generated during additive manufacturing (Yakin et al., 2021). These surface features may affect the material's electrochemical response and its susceptibility to localized corrosion in chloride-containing environments. In the present study, the anodic and cathodic behaviour of the APed (AP) and SPed (SP6, SP8, and SP10) specimens was systematically evaluated to investigate the effect of SP on corrosion performance. The findings provide valuable insights into how post-processing surface modification enhances the corrosion resistance of LPBF 316L SS, thereby improving its suitability for biomedical implant applications.

3.3.2 Open-Circuit Potential (OCP) Evolution and Stabilization

Figure 8 shows the OCP evolution of AP, SP6, SP8, and SP10 specimens during a 400 s exposure to 0.5 M NaCl. The OCP values stabilized at approximately −0.15 V for AP, −0.13 V for SP6, and −0.18 V for SP8 and SP10. AP exhibited a gradual negative shift from approximately −0.12 to −0.150 V, while SP6 remained comparatively stable within approximately −0.10 to −0.13 V, with only minor fluctuations, indicating stabilization of the metal/electrolyte interface before subsequent electrochemical measurements.

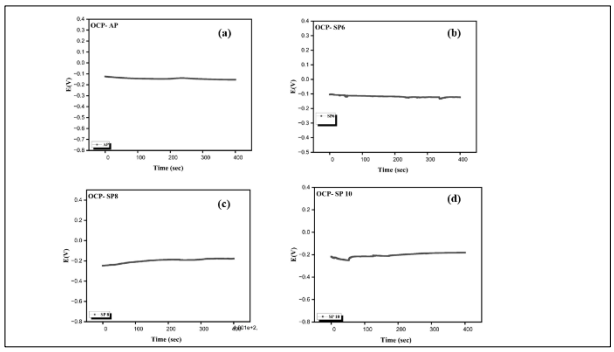


Figure 8. Open-circuit potential (OCP) evolution and stabilization of LPBF-fabricated 316L stainless steel in 0.5 M NaCl: (a) AP, (b) SP6, (c) SP8, and (d) SP10 specimens

In contrast, SP8 and SP10 showed gradual ennoblement, with initial potentials of approximately −0.25 and −0.22 V rising to final values of approximately −0.18 and −0.18 V, respectively. This behaviour suggests interfacial adjustment and stabilization of the surface passive layer. However, OCP reflects only the electrochemical tendency of the metal/electrolyte interface and cannot independently quantify corrosion resistance. Therefore, corrosion performance is further evaluated using potentiodynamic polarization and EIS parameters, particularly the corrosion current density and charge-transfer resistance.

3.3.3 Potentiodynamic polarization (PDP) measurement

The potentiodynamic polarization (PDP) test was employed to evaluate the corrosion behaviour of LPBF-fabricated 316L SS under APed and SPed conditions in 0.5 M NaCl solution. The corresponding Tafel polarization curves are presented in Figure 9, while the electrochemical parameters, including corrosion potential (E_{corr}), corrosion current density (I_{corr}), and corrosion rate (R_{corr}), are summarized in Table 5. Compared with the AP sample, the SPed specimens showed progressively lower corrosion current densities (I_{corr}) and corrosion rates (R_{corr}), indicating improved corrosion resistance with increasing shot-peening duration.

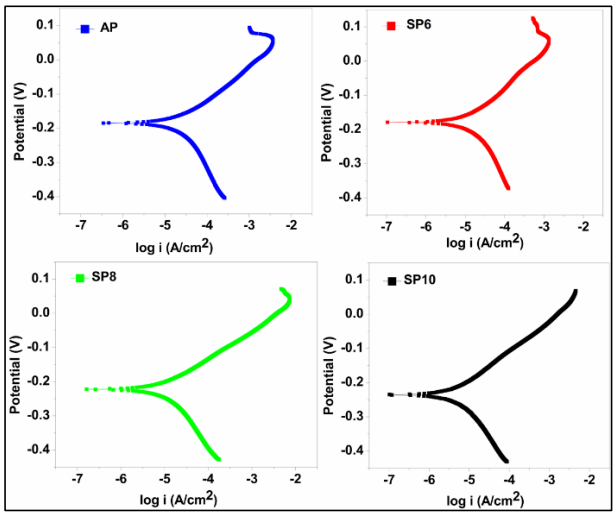


Figure 9. Potentiodynamic polarization (Tafel) curves of LPBF 316L SS samples in the as-printed (AP) and shot-peened conditions (SP6, SP8, and SP10) after 6, 8, and 10 min of shot peening, respectively

Table 5. Electrochemical corrosion parameters of as-printed (AP) and shot-peened (SP6, SP8, and SP10) LPBF 316L SS samples obtained experimentally by Tafel fitting of PDP curves

Sample	AP	SP6	SP8	SP10
Corrosion Potential, E_{corr} (mV)	-186.7	-179.0	-222.0	-235.2
Corrosion current density, I_{corr} (μA/cm^2)	19.68±0.96	14.17±0.90	10.51±0.89	4.65±0.36
$+\beta_a$ (mV dec^{-1})	206.65	162.81	174.06	126.87
$-\beta_c$ (mV dec^{-1})	97.72	111.35	85.79	92.72
Corrosion rate, R_{corr} (mpy)	8.907±1.02	6.414±0.29	4.757±0.48	2.103±0.55

The improved electrochemical performance of the SPed samples is attributed to the surface modifications induced by SP. As evidenced by the SEM observations of the microstructure discussed in Section 3.1, SP progressively reduced surface porosity and refined the microstructure through severe plastic deformation. This process generated ultrafine grains, increased grain boundary and dislocation densities, and introduced compressive residual stresses, as reported in the authors' previous work (MariyaDas & Naidu, 2026). These microstructural features may promote a more favorable surface condition for passivation, thereby limiting electrochemical dissolution and enhancing corrosion resistance, consistent with observations reported by Yakin et al. (2021). In contrast, the AP sample exhibited inferior corrosion behavior due to its rough surface morphology, residual porosity, tensile residual stresses inherited from the LPBF process, coarse grain structure, and relatively

lower surface and subsurface hardness. These characteristics promote localized electrochemical reactions, resulting in a lower E_{corr}, higher I_{corr}, and consequently a higher corrosion rate (Kong et al., 2019).

Accordingly, the corrosion resistance of the investigated specimens followed the order SP10 > SP8 > SP6 > AP. This trend is further supported by the corrosion current density (I_{corr}) and corrosion rate (R_{corr}) values shown in Figure 10 and Table 5.

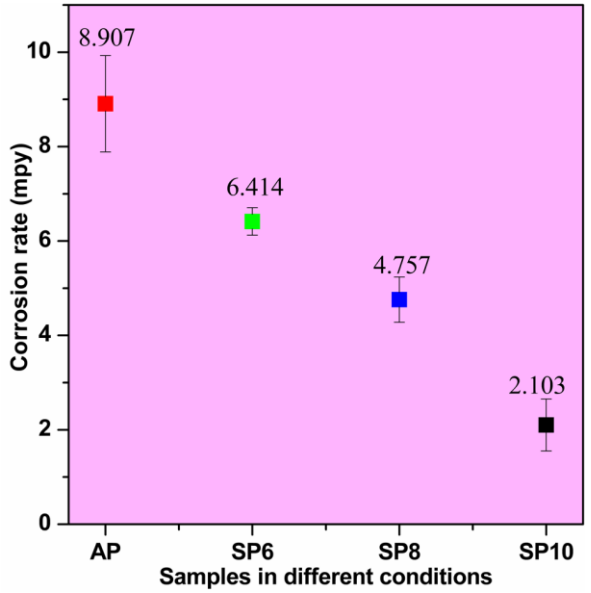


Figure 10. Experimentally determined corrosion rates of as-printed (AP) and shot-peened (SP6, SP8, and SP10) LPBF 316L SS samples, derived from PDP measurements

I_{corr} decreased progressively from 19.68 ± 0.96 µA/cm² for AP to 14.17 ± 0.90, 10.51 ± 0.89, and 4.65 ± 0.36 µA/cm² for SP6, SP8, and SP10, respectively. Consistent with this reduction in I_{corr}, the corresponding R_{corr} decreased from 8.907 ± 1.02 mpy for AP to 6.414 ± 0.29, 4.757 ± 0.48, and 2.103 ± 0.55 mpy for SP6, SP8, and SP10, respectively. The concurrent decrease in I_{corr} and R_{corr} with longer shot-peening durations suggests a gradual decline in the corrosion activity of the LPBF 316L SS surface. Notably, SP10 shows the lowest corrosion current density and rate among all tested conditions. Conversely, the SP8 sample achieves the highest microhardness after 8 minutes of shot peening, along with lower surface roughness compared to the AP and SP6 conditions, as noted in the authors' previous work (MariyaDas & Naidu, 2026). Although SP8 offers a good balance of surface roughness and microhardness, extending the shot-peening to 10 minutes yields the best overall electrochemical corrosion resistance. These results demonstrate that higher microhardness does not always equate to improved corrosion resistance. This superior behaviour may be attributed to the combined effects of modified surface roughness, microstructural refinement, compressive residual stresses, enhanced surface and subsurface hardness, and favorable surface conditions that may support improved passivation after 10 min of shot peening. Previous studies indicate that shot-peening-induced surface hardening and compressive residual stresses can significantly influence the corrosion response of 316L stainless steel. Alharbi (2023) reported an approximately 120% improvement in the corrosion resistance of additively manufactured 316L SS after ultrasonic shot peening in a 0.35 M NaCl solution, attributing this enhancement to increased microhardness and compressive residual stresses. However, excessive or severe shot peening may introduce high residual stresses, dislocations, and substantial near-surface deformation, which can compromise passive-film stability and thereby limit further improvements in the corrosion resistance of additively manufactured 316L stainless steel.
Behjat et al. (2023) reported that shot peening of LPBF-fabricated 316L stainless steel modifies surface morphology, microstructure, and residual stresses, thereby influencing the electrochemical response and improving resistance to pitting and polarization.

Compared with the AP specimen, SP improved the microstructural homogeneity of LPBF 316L stainless steel by refining the surface, reducing defects and the influence of melt pool boundaries, and introducing beneficial compressive residual stresses. These modifications promoted the formation of a more stable passive film, thereby enhancing corrosion resistance as reported in the authors' works (Alharbi, 2023; Santa-Aho et al., 2021).

Therefore, the corrosion behaviour of LPBF-fabricated 316L SS may be influenced by the combined effects of surface roughness, microstructural refinement, residual stress state, and surface hardness, all of which are modified to varying degrees by shot peening.

Additionally, a scan rate of 10 mV/s was selected and applied consistently to all specimens to ensure a direct comparison of their electrochemical behavior under identical conditions, while limiting prolonged surface exposure to the chloride electrolyte during polarization. Although a slower scan rate could provide further insight into passive-film stabilization, the consistent application of 10 mV/s allows reliable evaluation of the relative improvement in corrosion resistance produced by shot peening.

3.3.4 Electrochemical impedance spectroscopy (EIS) measurement

Electrochemical impedance spectroscopy (EIS) is a powerful technique for evaluating the corrosion behaviour of stainless steels by characterizing the electrochemical properties of the passive film and the metal/electrolyte interface (Santa-Aho et al., 2021). The Nyquist plots obtained from the EIS measurements exhibit semicircular capacitive arcs in the high- to medium-frequency region for all investigated specimens.

The diameter of the capacitive semicircle is directly related to the charge-transfer resistance (R_{ct} *or* R_p), which reflects the material's corrosion resistance.

The diameter of the capacitive semicircle is directly related to the charge-transfer resistance (R_{ct} *or* R_p), which reflects the material's corrosion resistance. Consequently, a larger semicircular arc corresponds to a higher charge-transfer resistance, indicating the formation of a more protective passive film and enhanced corrosion resistance (Balusamy et al., 2010; Man et al., 2019). Nyquist plots in Figure 11 clearly compare SPed and APed samples. The arc radius trend (SP10>SP8>SP6>AP) suggests that the SP10 316L SS specimen likely has more stable passive layers, indicated by its largest arc radius.

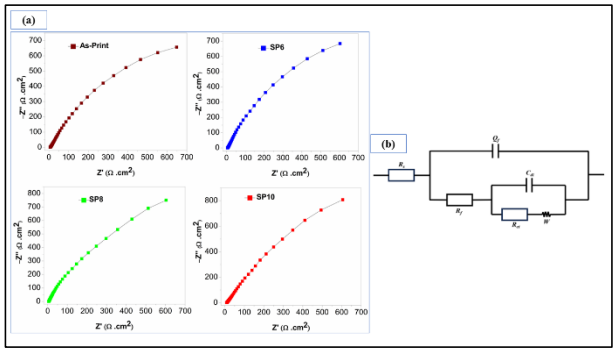


Figure 11. EIS characterization of LPBF 316L SS samples in the as-printed (AP) and shot-peened (SP6, SP8, and SP10) conditions: (a) Nyquist plots and (b) equivalent electrical circuit (EEC) model used for fitting the experimental EIS data.

As reported in another study, the larger diameter of the capacitive loop in the Nyquist plot suggests higher corrosion resistance (Radhamani et al., 2021). The same trend was observed in the PDP results across all shot-peening conditions, and the results were consistent with respect to corrosion resistance.

To further substantiate the corrosion behavior observed from the PDP measurements, Tafel curves, and Nyquist plots, the EIS data were analysed using the equivalent electrical circuit shown in Figure 11 (b). In this circuit, R_s represents the solution resistance; R_f and Q_f correspond to the resistance and capacitance of the passive surface film, respectively; R_{ct} denotes the charge-transfer resistance; C_{dl} represents the double-layer capacitance; and W is the Warburg impedance. The fitted electrochemical parameters obtained from the equivalent circuit are summarized in Table 6.

The AP specimen exhibited the lowest charge transfer resistance (R_{ct}) of 2378 Ω·cm². In contrast, SP produced a marked increase in R_{ct}, with values of 4195 Ω·cm², 5604 Ω·cm², and 10100 Ω·cm² for the SP6, SP8, and SP10 specimens, respectively.

Table 6. Equivalent electrical circuit (EEC) fitting parameters derived from experimental EIS data for as-printed (AP) and shot-peened (SP6, SP8, and SP10) LPBF 316L SS samples

Sample	AP	SP6	SP8	SP10
R_s (Ωcm^2)	5.567	8.989	4.534	7.551
Y_0 (10^{-5})	7.44	9.056	0.5749	17.74
n	0.7978	0.7477	0.9666	0.69
R_f (Ω cm^2)	6.049	5.612	5.524	31.16
Y_0 (10^{-5})	14.05	17.03	45.85	12.68
n	0.7626	0.7288	0.6159	0.6705
R_{ct} (Ωcm^2)	2378	4195	5604	10100
R_p	2442.6	4209.53	5614.05	10,138.71
W	1.141e11	9.308e7	2.557e6	4.431e5
C_{dl} (μFcm^2)	48.29	65.4	51.06	230.9

Consequently, the corrosion resistance followed the order SP10 > SP8 > SP6 > AP, consistent with the trends observed from the PDP and Nyquist analyses. The substantial increase in *Rct* after SP indicates greater resistance to interfacial charge transfer, which may result from suppressing anodic metal dissolution and could improve the stability of the passive film. Among all the specimens, the SP10 sample exhibited the highest R_{ct}, demonstrating the most effective corrosion protection.

The superior electrochemical performance of the SP10 specimen is primarily attributed to the multi-scale surface modifications induced by SP—specifically, better surface roughness, localized grain refinement, and the introduction of deep compressive residual stresses. Mechanistically, the significantly lower corrosion rate observed after 10 min of shot peening may be associated with the combined effects of subsurface mechanical densification, including pore closure reported in the authors' previous work (Mariya Das & Naidu, 2026), and the induced compressive residual stresses, which together may lead to a more favorable electrochemical response. The improved corrosion response observed after shot peening may therefore be associated with the combined effects of surface modification and microstructural refinement. Chen et al. (2020) reported a similar relationship between reduced surface roughness, grain refinement, and enhanced corrosion resistance in post-processed LPBF 316L stainless steel.

Consequently, these structural modifications minimized susceptibility to localized corrosion, thereby granting the SP10 condition the highest corrosion resistance among all investigated specimens.

These findings are broadly consistent with those reported by Behjat et al. (2023), who observed improved electrochemical corrosion performance in shot-peened LPBF-fabricated AISI 316L stainless steel, as evidenced by a wider passive range in potentiodynamic polarization and higher polarization resistance in EIS analysis. The present EIS results similarly indicate an improved corrosion response after surface treatment, although passive-film characteristics were not directly evaluated in this study.

EIS measurements spanned 100 kHz to 1 Hz, chosen to enable consistent comparison of interfacial electrochemical responses and charge-transfer features of the specimens. Lower frequencies (like 0.01 Hz) could reveal slow passive-film and diffusion processes, but the selected range was adequate for comparing electrochemical behavior, which was investigated in this study. The increase in charge-transfer resistance with shot-peening, along with reduced corrosion rates from PDP, shows improved corrosion resistance with longer shot-peening duration.

3.3.5 Bode Impedance and Phase-Angle Response

Figure 12 presents the Bode impedance-magnitude (|Z|) and phase-angle responses of the AP, SP6, SP8, and SP10 specimens. In the impedance-magnitude plot, the AP specimen exhibits the lowest |Z| response, whereas shot peening progressively increases the impedance, with SP10 showing the highest magnitude, followed by SP8 and SP6, particularly toward the intermediate-to-lower measured frequencies.

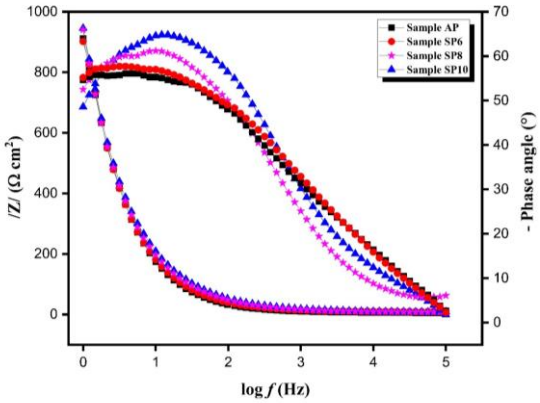


Figure 12. Bode plots showing impedance magnitude (|Z|) and phase-angle responses for AP, SP6, SP8, and SP10 LPBF-fabricated 316L stainless steel specimens in 0.5 M NaCl

This trend is consistent with the Nyquist plots and EEC-derived resistance values. The phase-angle plot also distinguishes the surface conditions: AP shows a comparatively narrower phase response, while the shot-peened specimens, particularly SP8 and SP10, exhibit a broader phase-angle region, indicating a more pronounced non-ideal capacitive response at the metal/electrolyte interface.

The broad phase response and depressed Nyquist arcs support the use of a constant-phase element (CPE) to account for surface heterogeneity and frequency dispersion. Overall, the Bode results corroborate the improved interfacial corrosion resistance after shot peening, with SP10 exhibiting the strongest impedance response. However, because the EIS measurements were limited to 100 kHz–1 Hz, the results are interpreted comparatively rather than as a complete characterization of low-frequency passive-film or diffusion-controlled processes.

3.3.6 SEM–EDS Analysis of Corrosion Morphology

Post-corrosion FESEM–EDS examination revealed distinct variations in the surface morphology and elemental distribution of the AP and shot-peened LPBF 316L stainless steel specimens after electrochemical exposure to 0.5 M NaCl, as shown in Figure 13. These observations are discussed alongside the corresponding electrochemical results to assess the influence of shot-peening-induced surface modifications on the corrosion response. Similar relationships among surface condition, post-processing, and the corrosion behavior of 316L stainless steel have been reported in prior studies (Lodhi et al., 2018; Over & Yao, 2025; Walczak et al., 2024).

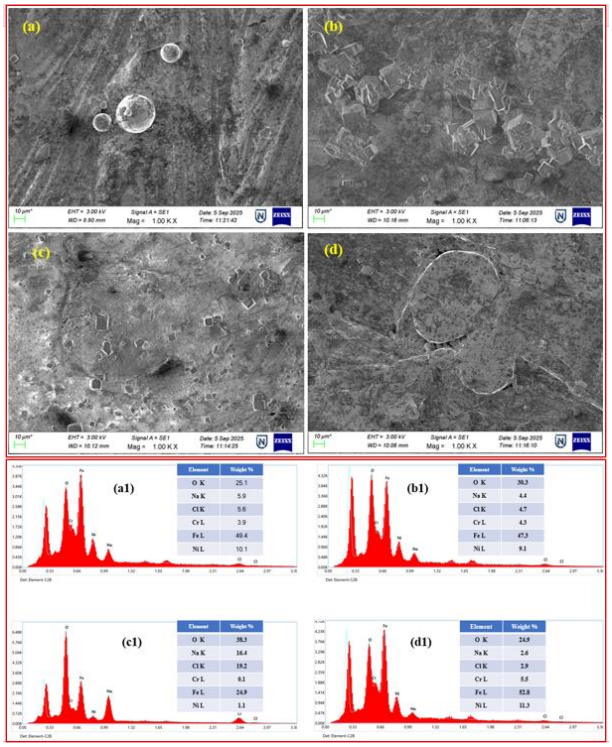


Figure 13. Post-corrosion SEM micrographs of LPBF 316L SS samples under (a) AP, (b) SP6, (c) SP8, and (d) SP10 conditions, with the corresponding EDS spectra (a1–d1)

The AP specimen exhibits pronounced surface degradation, with irregular corrosion products and relatively deep surface depressions associated with the initially rough and heterogeneous LPBF surface (Figure 13a). Manufacturing-related surface features, including partially melted particles and irregular surface regions, remain evident. The corresponding EDS spectrum (Figure 13a1) shows Fe, O, and Cl as the major detected elements, with wt.% of 49.4, 25.1, and 5.6, respectively. The presence of Cl on the exposed surface indicates chloride accumulation following immersion.

After 6 min of shot peening, the SP6 specimen shows a modified post-corrosion surface with less degradation and dispersed corrosion products (Figure 13b). Shot-peening plastically deforms the surface and changes asperity morphology. EDS analysis (Figure 13b1) reveals increased oxygen to 30.3 wt.% and decreased Cl to 4.7 wt.%, indicating surface composition differences after corrosion compared to the AP condition. However, EDS results only show surface composition and do not confirm the formation, thickness, continuity, or protective qualities of any surface film.

The SP8 specimen shows a uniform post-corrosion surface with fewer degradation features than AP and SP6 (Figure 13c). Its EDS spectrum (Figure 13c1) indicates higher oxygen (38.3 wt.%) and lower Fe (24.9 wt.%) contents, reflecting the corrosion products. However, EDS alone cannot determine the chemical state or structure of these corrosion products, so no specific oxide phase is assigned.

Among the investigated conditions, the SP10 specimen exhibits the least pronounced visible surface degradation after corrosion exposure (Figure 13d). No extensive regions of severe surface damage are observed within the examined FESEM field. The EDS spectrum (Figure 13d1) shows a relatively low Cl content of 2.9 wt.% and Cr and Ni contents of 5.5 and 11.3 wt.%, respectively. The elemental distribution indicates differences in post-corrosion surface chemistry compared with the other conditions. The relatively lower detected Cl content may indicate reduced chloride retention on the examined surface; however, this observation alone does not establish the mechanism responsible for the improved corrosion behaviour.

Overall, the FESEM and EDS observations demonstrate a progressive change in post-corrosion surface morphology and elemental composition with increasing shot-peening duration. The reduction in severe surface degradation features and the changes in Fe, O, Cr, Ni, and Cl contents are consistent with the improved electrochemical corrosion response observed for the shot-peened specimens. The results suggest that shot peening modifies the surface condition and consequently influences its response to the chloride-containing environment. However, the present SEM/EDS analysis does not provide direct evidence for specific passive-film compositions, Cr_2O_3 formation, pore closure, microcrack removal, or grain-refinement-driven diffusion mechanisms. Such mechanisms would require additional characterization, such as XPS, TEM, or high-resolution cross-sectional analysis, and are therefore not claimed in the present study.

4. CONCLUSIONS

This study systematically investigated the effects of shot peening on the surface characteristics, wettability, and corrosion behaviour of LPBF-fabricated 316L stainless steel. The major findings are summarized as follows:

1. Shot peening significantly modified the surface morphology and microstructure through severe plastic deformation, producing overlapping indentations, grain refinement, and compressive residual stresses. Consequently, the surface roughness (R_z) decreased from 107.81±6.47µm (AP) to 73.35±3.67µm (SP6) and 68.39±3.08µm (SP8), then increased slightly to 70.79±3.54µm (SP10) due to excessive peening-induced surface damage and indentation overlap.
2. Shot peening altered the wettability of LPBF-fabricated 316L stainless steel. In PBS, the contact angle increased from 73.08 ± 2.84° (AP) to 88.60 ± 3.10° (SP8), then slightly decreased to 84.07 ± 2.62° (SP10), whereas in DI water it initially decreased to a minimum at SP6 (26.23 ± 1.85°) and then increased up to SP10 (75.26±2.78°). Nevertheless, all specimens exhibited contact angles below 90°, confirming the retention of hydrophilic surfaces suitable for biomedical applications.
3. Electrochemical analysis confirmed improved corrosion resistance of LPBF 316L stainless steel after shot peening. OCP showed interfacial stabilization within 400 s, while the corrosion rate decreased from 8.907 ± 1.02 mpy (AP) to 6.414 ± 0.29 (SP6), 4.757 ± 0.48 (SP8), and 2.103 ± 0.55 mpy (SP10). EIS showed increased charge-transfer resistance, reaching ~10,100 Ω·cm² for SP10, while Bode plots supported this trend through higher impedance magnitude and broader phase-angle responses after shot peening. Together with post-corrosion FESEM–EDS observations, the OCP, PDP, Nyquist/EEC, and Bode results establish the corrosion-resistance order SP10 > SP8 > SP6 > AP, with SP10 exhibiting the best performance in 0.5 M NaCl.
4. Overall, shot peening effectively modified the surface integrity, wettability, and corrosion resistance of LPBF-fabricated 316L stainless steel. Among the investigated conditions, SP8 exhibited the lowest surface roughness and the highest PBS contact angle, whereas SP10 showed the highest corrosion resistance. Therefore, the preferred shot-peening condition depends on the specific surface and electrochemical performance requirements, and the potential biomedical implications require further biological validation.

5. Future research may focus on integrating shot peening with advanced surface-modification techniques, such as laser shock peening, ultrasonic nanocrystal surface modification, or bioactive coatings, while also evaluating long-term in vitro and in vivo biocompatibility and tribo-corrosion performance to further enhance the clinical applicability of LPBF-fabricated 316L stainless steel implants. Advanced surface-characterization techniques, such as transmission electron microscopy (TEM), X-ray photoelectron spectroscopy (XPS), and Auger electron spectroscopy (AES), can also be employed to further investigate the composition, thickness, structure, and chemical state of the passive layer formed on the corroded specimens.

Acknowledgments: The authors sincerely thank J. Venumurali, Mulla Mahaboob Basha, J.M. Babu, C. Srinivasa Reddy, and M. Ramesh Naik for their valuable assistance during the experimentation and data analysis. The authors also gratefully acknowledge the research scholars and Dr. Srilatha Rao of Nitte Meenakshi Institute of Technology, Bengaluru, for their support in conducting the electrochemical corrosion experiments and in data acquisition.

References:

Agrawal, A. K., & Thoma, D. J. (2022). High-throughput surface characterization to identify porosity defects in additively manufactured 316L stainless steel. *Additive Manufacturing Letters*, *3*, 100093. https://doi.org/10.1016/j.addlet.2022.100093

Ahmed, A. A., Mhaede, M., Basha, M., Wollmann, M., & Wagner, L. (2015). The effect of shot peening parameters and hydroxyapatite coating on surface properties and corrosion behavior of medical grade AISI 316L stainless steel. *Surface and Coatings Technology*, *280*, 347–358. https://doi.org/10.1016/j.surfcoat.2015.09.026

Alharbi, N. (2023). Corrosion resistance of 3D printed SS316L post-processed by ultrasonic shot peening at optimum energy level. *Proceedings of the Institution of Mechanical Engineers, Part B: Journal of Engineering Manufacture*, *237*(5), 745–757. https://doi.org/10.1177/09544054221112164

ASTM F3184-16. (2024). *ASTM F3184-16: Standard Specification for Additive Manufacturing Stainless Steel Alloy (UNS S31603) with Powder Bed Fusion*. ASTM International. https://doi.org/10.1520/F3184-16

Aziz, U., McAfee, M., Manolakis, I., Timmons, N., & Tormey, D. (2025). A review of optimization of additively manufactured 316/316l stainless steel process parameters, post-processing strategies, and defect mitigation. *Materials*, *18*(12), 2870. https://doi.org/10.3390/ma18122870

Bae, K., Shin, D., Lee, J., Kim, S., Lee, W., Jo, I., & Lee, J. (2022). Corrosion resistance of laser powder bed fused AISI 316L stainless steel and effect of direct annealing. *Materials*, *15*(18), 6336. https://doi.org/10.3390/ma15186336

Bagehorn, S., Wehr, J., & Maier, H. J. (2017). Application of mechanical surface finishing processes for roughness reduction and fatigue improvement of additively manufactured Ti-6Al-4V parts. *International Journal of Fatigue*, *102*, 135–142. https://doi.org/10.1016/j.ijfatigue.2017.05.008

Bagherifard, S., Ghelichi, R., Khademhosseini, A., & Guagliano, M. (2014). Cell response to nanocrystallized metallic substrates obtained through severe plastic deformation. *ACS Applied Materials & Interfaces*, *6*(11), 7963–7985. https://doi.org/10.1021/am501119k

Bagherifard, S., Hickey, D. J., De Luca, A. C., Malheiro, V. N., Markaki, A. E., Guagliano, M., & Webster, T. J. (2015). The influence of nanostructured features on bacterial adhesion and bone cell functions on severely shot peened 316L stainless steel. *Biomaterials*, *73*, 185–197. https://doi.org/10.1016/j.biomaterials.2015.09.019

Balusamy, T., Kumar, S., & Sankara Narayanan, T. S. N. (2010). Effect of surface nanocrystallization on the corrosion behaviour of AISI 409 stainless steel. *Corrosion Science*, *52*(11), 3826–3834. https://doi.org/10.1016/j.corsci.2010.07.004

Barberi, J., & Spriano, S. (2021). Titanium and protein adsorption: An overview of mechanisms and effects of surface features. *Materials*, *14*(7), 1590. https://doi.org/10.3390/ma14071590

Barode, J., Brander, M., Yu, T., Nadimpalli, V. K., Jensen, D. J., & Wang, X. (2025). Cell structure in lpbf 316l—Microstructural heterogeneity, thermal stability, and mechanical properties. *Materials*, *18*(3), 475. https://doi.org/10.3390/ma18030475

Basha, M. M., & Sankar, M. R. (2023). Experimental investigations on surface morphology and metallurgical studies of additive manufactured stainless steel features finished by electrolytic ionic interactions. *Tribology International*, *188*, 108776. https://doi.org/10.1016/j.triboint.2023.108776

Basha, S. M., Venkaiah, N., Srivatsan, T. S., & Sankar, M. R. (2024). A review on severe plastic deformation based post-processes for metal additive manufactured complex features. *Materials and Manufacturing Processes*, *39*(3), 291–309. https://doi.org/10.1080/10426914.2023.2244033.

Behjat, A., Shamanian, M., Taherizadeh, A., Lannunziata, E., Bagherifard, S., Gadalińska, E., Saboori, A., & Iuliano, L. (2023). Microstructure-electrochemical behavior relationship in post processed AISI316L stainless steel parts fabricated by laser powder bed fusion. *Journal of Materials Research and Technology, 23*, 3294–3311. https://doi.org/10.1016/j.jmrt.2023.01.229

Chabak, Y., Efremenko, B., Petryshynets, I., Efremenko, V., Lekatou, A. G., Zurnadzhy, V., Bogomol, I., Fedun, V., Kovaľ, K., & Pastukhova, T. (2021). Structural and tribological assessment of biomedical 316 stainless steel subjected to pulsed-plasma surface modification: Comparison of lpbf 3d printing and conventional fabrication. *Materials*, *14*(24), 7671. https://doi.org/10.3390/ma14247671

Chen, L., Richter, B., Zhang, X., Ren, X., & Pfefferkorn, F. E. (2020). Modification of surface characteristics and electrochemical corrosion behavior of laser powder bed fused stainless-steel 316L after laser polishing. *Additive Manufacturing, 32*, 101013. https://doi.org/10.1016/j.addma.2019.101013

Chen, M., Deng, W., Li, J., Jiang, C., & Ji, V. (2025). Study on surface characteristics and wear resistance of PBF-LB Ti-6Al-4V alloy treated by shot peening. *Materials Today Communications*, *46*, 112901. https://doi.org/10.1016/j.mtcomm.2025.112901

DebRoy, T., Wei, H. L., Zuback, J. S., Mukherjee, T., Elmer, J. W., Milewski, J. O., Beese, A. M., Wilson-Heid, A., De, A., & Zhang, W. (2018). Additive manufacturing of metallic components – Process, structure and properties. *Progress in Materials Science*, *92*, 112–224. https://doi.org/10.1016/j.pmatsci.2017.10.001

Diaz Vallejo, N., Lucas, C., Ayers, N., Graydon, K., Hyer, H., & Sohn, Y. (2021). Process optimization and microstructure analysis to understand laser powder bed fusion of 316l stainless steel. *Metals*, *11*(5), 832. https://doi.org/10.3390/met11050832

Frazier, W. E. (2014). Metal additive manufacturing: A review. *Journal of Materials Engineering and Performance*, *23*(6), 1917–1928. https://doi.org/10.1007/s11665-014-0958-z

Gibson, I., Rosen, D., Stucker, B., & Khorasani, M. (2021). *Additive manufacturing technologies*. Springer International Publishing. https://doi.org/10.1007/978-3-030-56127-7

Guillen, D., Wahlquist, S., & Ali, A. (2024). Critical review of lpbf metal print defects detection: Roles of selective sensing technology. *Applied Sciences*, *14*(15), 6718. https://doi.org/10.3390/app14156718

Haribaskar, R., & Sampath Kumar, T. (2024). Surface integrity of consecutive shot-peened additively manufactured 316L stainless steel. *Materials and Manufacturing Processes*, *39*(13), 1817–1829. https://doi.org/10.1080/10426914.2024.2368542

Jagannati, V., Gurram, M., Turaka, S., Naidu B, V. V., Verma, G. K., Krishnan, P. K., Sarimalla, R., Sebaey, T. A., & Bandaru, A. K. (2025). Review of tensile anisotropy in laser powder bed fusion 316L stainless steel: Build orientation effects and optimisation using machine learning. *Journal of Materials Research and Technology*, *38*, 5318–5341. https://doi.org/10.1016/j.jmrt.2025.08.249

Kirk, D. (1999). Shot peening. *Aircraft Engineering and Aerospace Technology*, *71*(4), 349–361. https://doi.org/10.1108/00022669910270727

Kirk, D., & Coventry, I. (2012). An evolutionary guide to shot peening intensity measurement. *The Shot Peener*, Spring, 24–32.

Kong, D., Dong, C., Ni, X., Zhang, L., Yao, J., Man, C., Cheng, X., Xiao, K., & Li, X. (2019). Mechanical properties and corrosion behavior of selective laser melted 316L stainless steel after different heat treatment processes. *Journal of Materials Science & Technology*, *35*(7), 1499–1507. https://doi.org/10.1016/j.jmst.2019.03.003

Li, W., Meng, L., Niu, X., & Zhou, W. (2024). Microstructure, mechanical properties, and deformation behaviour of LPBF 316L via post-heat treatment. *Virtual and Physical Prototyping*, *19*(1), e2405623. https://doi.org/10.1080/17452759.2024.2405623

Lodhi, M. J. K., Deen, K. M., & Haider, W. (2018). Corrosion behavior of additively manufactured 316L stainless steel in acidic media. *Materialia*, *2*, 111–121. https://doi.org/10.1016/j.mtla.2018.06.015

Mahmood, M. A., Chioibasu, D., Ur Rehman, A., Mihai, S., & Popescu, A. C. (2022). Post-processing techniques to enhance the quality of metallic parts produced by additive manufacturing. *Metals*, *12*(1), 77. https://doi.org/10.3390/met12010077

Man, C., Dong, C., Liu, T., Kong, D., Wang, D., & Li, X. (2019). The enhancement of microstructure on the passive and pitting behaviors of selective laser melting 316L SS in simulated body fluid. *Applied Surface Science*, *467–468*, 193–205. https://doi.org/10.1016/j.apsusc.2018.10.150

MariyaDas, G., & Naidu, B. V. V. (2026). Shot peening effects on the surface and structural characterization, fatigue performance and tribological behavior of additive manufactured stainless steel 316l features. *Journal of Materials Engineering and Performance*, *35*(15), 14955–14974. https://doi.org/10.1007/s11665-025-12683-4

Mofazali, P., Dustmohamadi, Z., Atapour, M., Sheikholeslam, M., Saboori, A., & Iuliano, L. (2025). Tailoring surface characteristics of laser powder bed fusioned AISI 316L stainless steel for biomedical applications. *Progress in Additive Manufacturing*, *10*(8), 5009–5024. https://doi.org/10.1007/s40964-024-00882-9

Nizam, M., Purohit, R., & Taufik, M. (2024). Materials for 3D printing in healthcare sector: A review. *Proceedings of the Institution of Mechanical Engineers, Part H: Journal of Engineering in Medicine*, *238*(10), 939–963. https://doi.org/10.1177/09544119241289731

Over, V., & Yao, Y. L. (2025). Effect of laser shock peening on electrochemistry and wettability of additively manufactured stainless steel. *Journal of Manufacturing Science and Engineering*, *147*(3), 031008. https://doi.org/10.1115/1.4065022

Radhamani, A. V., Lau, H. C., & Ramakrishna, S. (2021). 316l stainless steel microstructural, mechanical, and corrosion behavior: A comparison between spark plasma sintering, laser metal deposition, and cold spray. *Journal of Materials Engineering and Performance*, *30*(5), 3492–3501. https://doi.org/10.1007/s11665-021-05571-0

Sangoi, K., Nadimi, M., Song, J., & Fu, Y. (2025). Heat treatment effect on the corrosion resistance of 316l stainless steel produced by laser powder bed fusion. *Metals*, *15*(1), 41. https://doi.org/10.3390/met15010041

Santa-Aho, S., Kiviluoma, M., Jokiaho, T., Gundgire, T., Honkanen, M., Lindgren, M., & Vippola, M. (2021). Additive manufactured 316l stainless-steel samples: Microstructure, residual stress and corrosion characteristics after post-processing. *Metals*, *11*(2), 182. https://doi.org/10.3390/met11020182

Smeets, R., Stadlinger, B., Schwarz, F., Beck-Broichsitter, B., Jung, O., Precht, C., Kloss, F., Gröbe, A., Heiland, M., & Ebker, T. (2016). Impact of dental implant surface modifications on osseointegration. *BioMed Research International*, *2016*, 1–16. https://doi.org/10.1155/2016/6285620

Sun, F., Adachi, Y., Sato, K., Ishimoto, T., Nakano, T., & Koizumi, Y. (2024). Delineating the ultra-low misorientation between the dislocation cellular structures in additively manufactured 316l stainless steel. *Materials*, *17*(8), 1851. https://doi.org/10.3390/ma17081851

Sun, Z., Tang, C., Soh, V., Lee, C., Wu, X., Sing, S. L., Liu, A. Z., Wei, S., Zhou, K., Tan, C. C., Wang, P., & Chua, C. K. (2024). Laser powder bed fusion of 316L stainless steel and K220 copper multi-material. *Virtual and Physical Prototyping*, *19*(1), e2356078. https://doi.org/10.1080/17452759.2024.2356078

Thangaraj, B., T. S. Nellaiappan, S. N., Kulandaivelu, R., Lee, M. H., & Nishimura, T. (2015). A facile method to modify the characteristics and corrosion behavior of 304 stainless steel by surface nanostructuring toward biomedical applications. *ACS Applied Materials & Interfaces*, *7*(32), 17731–17747. https://doi.org/10.1021/acsami.5b03877

Venumurali, J., Reddy, B. S., Turaka, S., Ragupathy, V. D., & Reddy, P. S. (2024). Effects of peening duration on surface and wear properties of aircraft graded AA2017 alloy. *Surface and Coatings Technology*, *477*, 130361. https://doi.org/10.1016/j.surfcoat.2023.130361

Venumurali, J., Turaka, S., SanthaRao, D., Krishnan, P. K., Tirumala, T., Ravindra, K., Rajesh, K., Pappula, B., & Makgato, S. (2025). Computation of structural parameters developed by shot peening and their influence on residual stress and wear properties of AA2017 alloy. *Journal of Alloys and Compounds*, *1036*, 181650. https://doi.org/10.1016/j.jallcom.2025.181650

Walczak, M., Matijošius, J., Özkan, D., & Pasierbiewicz, K. (2024). Effect of shot peening parameters on surface properties and corrosion resistance of 316l stainless steel. *Advances in Science and Technology Research Journal*, *18*(3), 296–304. https://doi.org/10.12913/22998624/186513

Yadroitsev, I., & Smurov, I. (2011). Surface morphology in selective laser melting of metal powders. *Physics Procedia*, *12*, 264–270. https://doi.org/10.1016/j.phpro.2011.03.034

Yakin, R. I., Iswanto, P. T., & Maliwemu, E. U. K. (2021). Shot peening effect on surface properties and pitting corrosion resistance of biomedical structural steel AISI 316L. *Metalurgija*, *60*(3–4), 249–252. https://hrcak.srce.hr/256002

Yazdani, F., Rabiee, S. M., & Jamaati, R. (2024). Comparison of conventional and severe shot peening effects on the microstructure, texture, roughness, hardness, and electrochemical behavior of austenitic stainless steel. *Heliyon*, *10*(10), e31284. https://doi.org/10.1016/j.heliyon.2024.e31284

Mariya Das Gurram
Mohan Babu University
Tirupati,
India
mariyadas2000@gmail.com
ORCID 0009-0006-3592-9620

Vishnu Vardhana Naidu B
Mohan Babu University
Tirupati,
India
vishnu234@gmail.com
ORCID 0000-0001-8971-2255